

# Shielding data for 100–250 MeV proton accelerators: Double differential neutron distributions and attenuation in concrete

S. Agosteo<sup>a</sup>, M. Magistris<sup>b</sup>, A. Mereghetti<sup>a,b,\*</sup>, M. Silari<sup>b</sup>, Z. Zajacova<sup>b,c</sup>

<sup>a</sup> Polytechnic of Milano, Department of Nuclear Engineering, Via Ponzio 34/3, 20133 Milano, Italy

<sup>b</sup> CERN, 1211 Geneve 23, Switzerland

<sup>c</sup> Slovak University of Technology, Ilkovičova 3, 81219 Bratislava, Slovak Republic

Received 27 June 2007; received in revised form 20 September 2007

Available online 7 October 2007

## Abstract

Double differential distributions of neutrons produced by 100, 150, 200 and 250 MeV protons stopped in a thick iron target were simulated with the FLUKA Monte Carlo code at four emission angles: forward, 45°, transverse and 135° backwards. The attenuation in ordinary concrete of the dose equivalent due to secondary neutrons, protons, photons and electrons was calculated. Some of the resulting attenuation curves are best fitted by a double-exponential function rather than a single-exponential. The effect of various approximations introduced in the simulations is thoroughly discussed. The contribution to the total ambient dose equivalent from photons and protons is usually limited to a few percent, except in the backward direction where photons contribute more than 10% and up to 35% to the total dose for a shield thickness of 1–2 m. Source terms and attenuation lengths are given as a function of energy and emission angle, along with fit to the Monte Carlo data. An extensive comparison is made of values obtained in the present work with published experimental and computational data.

© 2007 Elsevier B.V. All rights reserved.

PACS: 02.70.Uu; 87.53.Wz; 87.52.Ga; 87.53.–j

Keywords: Proton accelerator; Shielding; Dose equivalent; Attenuation length; Source term; Neutron double differential distribution

## 1. Introduction

Proton accelerators in the intermediate energy range (from a few tens to a few hundreds of MeV), in the past mainly used for nuclear physics research, since several years find increasing application in cancer radiation therapy. Several hospital-based facilities are being built or at the planning stage worldwide [1]. Machines in this energy range are also generally employed as injectors for high-energy accelerators (in the GeV region and above) at large research centres. An example is the 160 MeV linac presently being designed at CERN to replace the existing

50 MeV proton injector [2]. This accelerator is also intended to be the front-end of a 3.5 GeV superconducting proton linac for the production of intense neutrino beams for future neutrino physics experiments [3].

Shielding of these accelerators requires particular attention, either due to the large beam intensity required as injectors or, in the case of radiation therapy, because they are installed in a hospital, usually located in a highly populated area. The main radiation dictating the shielding requirements is the neutron field produced by the interaction of the proton beam with the structures of the accelerator, of the beam transfer lines and – in the case of medical machines – of the beam delivery system used to irradiate the patient (such as collimators and field-shaping devices), and with the patient himself (where the remaining beam is ultimately lost).

In shielding design it is often useful to perform a first assessment of the required shielding thickness by using a

\* Corresponding author. Address: Polytechnic of Milano, Department of Nuclear Engineering, Via Ponzio 34/3, 20133 Milano, Italy. Tel.: +39 02 2399 6318.

E-mail address: [alessio.mereghetti@mail.polimi.it](mailto:alessio.mereghetti@mail.polimi.it) (A. Mereghetti).

simplified approach based, for example, on a point-source line-of-sight model, to be verified at a more advanced stage of the project with a Monte Carlo simulation in a more realistic geometry of the facility. Handy data for simplified calculations are given for instance in [4]. Often this simplified approach provides a conservative estimate of the required shielding [5].

Shielding data in the intermediate energy range are not abundant in the literature and are usually limited to specific conditions, geometries and energy values. The shielding properties of materials, that is the attenuation length, varies rapidly with neutron energy in this range of energies [6]. To overcome this lack of information, this paper revises, updates and complements previous calculations with the aim of supplying shielding data for concrete (the most common material used in accelerator shielding). A forthcoming paper will provide the equivalent data for iron [7]. The present paper provides revised source terms and attenuation lengths as a function of proton energy and emission angle to be used in such estimates.

The attenuation through a shield made of ordinary concrete of the total dose equivalent produced by 100, 150, 200 and 250 MeV protons stopped in a thick iron target were calculated with the FLUKA Monte Carlo code [8,9] at four emission angles: forward, 45°, transverse and 135° backwards. The present calculations are meant to reproduce the dominant secondary radiation field created by a beam loss in a thick metallic target such as a magnet, a collimator or a vacuum chamber. Iron was chosen as representative of other materials of similar density and atomic number (such as copper and stainless steel), which are the main constituents of accelerator components. Shielding data for backward angles may also be of interest to account for special conditions found in modern hadron therapy facilities, where the beam extracted from the accelerator can be rotated 360° around the patient by means of a large mechanical structure (isocentric gantry). The dose equivalent behind the shield includes contribution from neutrons, photons, charged particles (protons and electrons) and their secondaries produced in the shielding material itself. The results of the calculations were fitted by the classical two-parameter formula of a point-source line-of-sight model. The results are compared with previous calculations and with recent literature data, and discrepancies are explained.

## 2. Monte Carlo simulations

The correct way to estimate the attenuation of radiation in a shield as a function of its thickness would be to per-

form individual sets of simulations for a series of slabs of different thicknesses placed at the given emission angle and to score the dose equivalent behind each slab. However, this process is very consuming in terms of computing time, as it requires a large number of simulations:  $N_{\text{total}} = N \times N_{\text{slab}} \times N_{\text{angle}}$ , where  $N$  is the number of simulations for each case, necessary to achieve statistical significance (typically  $N$  is in the range 5–10). In order to study different emission angles with a single geometry set-up, the present calculations were performed in a spherical geometry. Fourteen individual shield thicknesses and four emission angles were considered: forward, 45°, transverse and 135° backward. Separate simulations were dedicated to the backward angle to optimize the usage of CPU time.

### 2.1. FLUKA simulations

The simulations were performed with the latest version (Version 2006.03) of the FLUKA [8,9] Monte Carlo code. Secondary neutrons, photons, protons and electrons produced by a monoenergetic and monodirectional proton beam (“pencil beam”) impinging on an iron target located at the centre of a large spherical shield made of ordinary concrete (type TSF 5.5 Table 1), were transported in four angular bins with respect to the incident proton beam direction: 0–10° (forward), 40–50°, 80–90° (transverse) and 130–140° (backwards). Transport of secondary radiation was limited to these four angular bins by assigning “blackhole” (a material with infinite absorbency) to the bins in-between. The volume of the cavity delimited by the inner surface of the shield was filled with vacuum. The dose equivalent behind the shield was calculated offline by folding the fluence with the appropriate fluence to ambient dose equivalent conversion coefficients [10,11].

The target was cylindrical, with its axis coincident with the incoming beam direction, and it was slightly thicker than the proton range in iron at the given energy. After investigating various options for the target diameter (see below), the simulations were performed with targets with diameter equal to their length (right cylinder) because this choice ensures a sufficiently conservative combination between neutron yield and spectrum hardness.

The inner radius of the sphere was sufficiently large (90 m) to make curvature-related effects negligible. Simulations were run for 14 values of the shield thickness, up to 600 cm. The computed particle fluence was scored by means of inverse cosine-weighted boundary crossing estimators (i.e. fluence across a surface) at the interface between shielding and the outside blackhole, taking into account only particle fluences directed outwards (“one-

Table 1  
Elemental composition, percent water content and density of concrete TSF-5.5

Elemental composition ( $10^{21}$ atoms $\text{cm}^{-3}$ )								Water content (by weight)	Density ( $\text{g cm}^{-3}$ )
H	C	O	Mg	Al	Si	Ca	Fe		
8.5	20.2	35.5	1.86	0.6	1.7	11.3	0.19	5.5%	2.31

way” scoring option). Variance reduction techniques were used, namely “geometry splitting” and “Russian roulette”. Each region importance was adjusted so as to maintain the number of particles approximately constant throughout the shield. Each data point is the average of the results of at least 10 independent simulations. The total number of histories per data point was at least 2,000,000.

## 2.2. Preliminary simulations

In order to better reproduce reality, the FLUKA geometry was made such as to minimize the following three effects:

- Neutron exchange between contiguous angular bins during transport.
- Neutron scattering back and forth across a boundary estimator during transport (typical of neutron scoring inside an homogeneous medium and not occurring while scoring outside a shield, that is at the interface between the shield material and air).
- Neutron transport in one angular bin after being back-scattered from another angular bin (“cross-talk” from the inner surface of the sphere), as shown in Fig. 1.

In order to evaluate the importance of these effects, a number of preliminary simulations were run:

- For proton energies of 100 MeV and 250 MeV: neutrons were transported in all 18 angular bins (in three sets of simulations, from 0–10° to 70–80°, from 50–60° to 130–140°, and from 100–110° to 170–180°) and scored inside the shield every 20 cm (“full sphere”) for a total of 26 depth values.

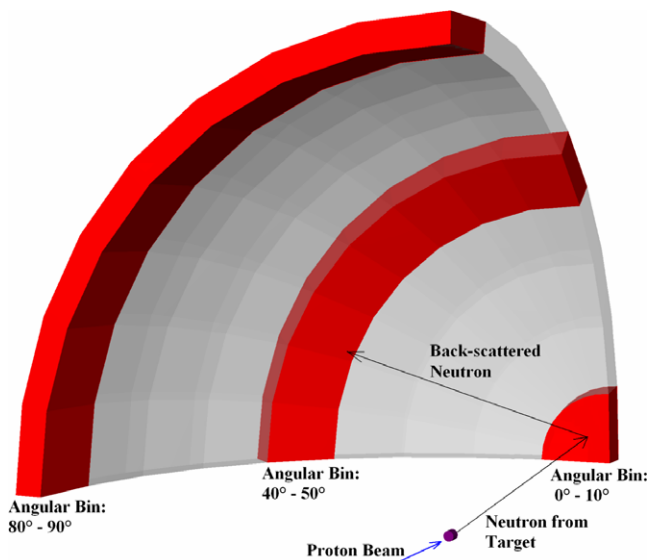


Fig. 1. Example of neutron “cross-talk” from the inner surface of the sphere.

- For proton energies of 100 MeV and 250 MeV: neutrons were transported in the 0–10°, 40–50°, 80–90° and 140–150° (130–140° for 250 MeV) angular bins and scored inside the shield every 20 cm (“selected bins”) for 26 depths.
- For 250 MeV proton energy: neutrons were transported only in the 80–90° angular bin and scored outside the shield, for 14 individual concrete thicknesses (“shell per shell” case). Further preliminary simulations were carried out to describe how the target dimensions can influence the neutron spectrum and its attenuation through a concrete shield.
- For 250 MeV proton energy: the neutron spectrum was scored for four target dimensions in all 18 angular bins between 0° and 180°.
- For 250 MeV proton energy: neutrons produced in an iron target 7.5 cm in radius and 15 cm in length were transported through concrete in the 0–10°, 40–50° and 80–90° angular bins and scored outside the shield, for 14 individual concrete thicknesses.

For these preliminary simulations, the attenuation parameters were obtained by fitting the data with the least square method using expression (1) given in Section 4, between 200 cm and 560 cm depth. Results beyond 560 cm are of no statistical significance. The uncertainties on attenuation length and source term are the pure statistical uncertainties due to the fit.

Figs. 2 and 3 compare cases 1) and 2) at 0–10°, 40–50°, 80–90° and 140–150° (130–140°) for 100 MeV and 250 MeV protons, respectively. This comparison shows the contribution to the total dose of neutron scattering between contiguous angular bins. At 100 MeV the data for the full sphere are consistent with those for the selected angular bins within 15% at 0–10° and within 10% at 40–50° and 80–90°. For these bins the attenuation length for the “full sphere” case is 2% larger than for the “selected bins”

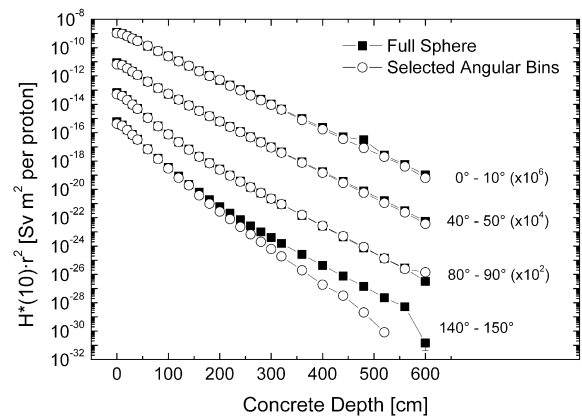


Fig. 2. Attenuation in ordinary concrete of the total dose equivalent produced by 100 MeV protons on a thick iron target: comparison of the results from simulations with the “full sphere” and with individual angular bins.

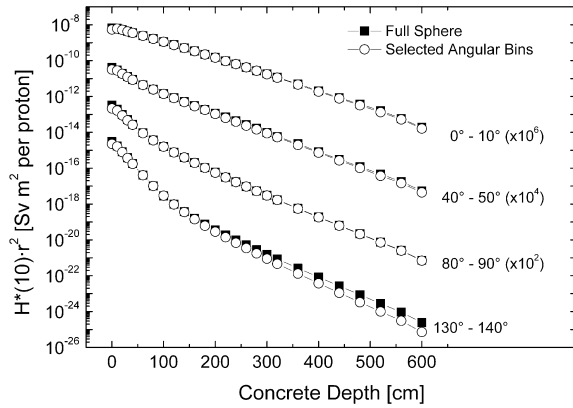


Fig. 3. Attenuation in ordinary concrete of the total dose equivalent produced by 250 MeV protons on a thick iron target: comparison of the results from simulations with the “full sphere” and with individual angular bins.

case. This is a marginal difference when compared to the statistical uncertainties of the simulations, which are typically less than 10% except at the largest depths where they reach 15% at 80–90° and 40% at 140–150°. In the 140–150° region the neutron scattering between contiguous angular bins is enhanced. This can be due to a leakage of few high energy neutrons from smaller angular bins, as suggested by the slightly harder slope of the attenuation curve. Therefore the deviation between the two curves is much more evident and the fitting curves are actually rather different. For 250 MeV the two curves practically overlap up to 80–90° (the discrepancy is 6% at maximum) and the deviation at the backward angle is much less pronounced than at 100 MeV. The attenuation length for the “full sphere” is larger than the one obtained for the “selected bins” by, 2%, 1%, 0.3% and 9% for the 0–10, 40–50°, 80–90° and 130–140° bins, respectively. These values are to be compared with statistical uncertainties of the simulated data of the order of 5%. The typical statistical uncertainty on the source term ranges from 2% to 12% at 100 MeV and from 1% to 6% at 250 MeV. For the attenuation length the statistical uncertainties are always below 1%. In general at any given angle the average energy of the neutron spectrum increases with proton energy and therefore the difference between the “full sphere” and the “selected bins” cases reduces with increasing proton energy. One can state that simulations with a few selected angular bins do not “perturb” significantly the geometry with respect to the simulations with the full sphere, except at the lowest energy and at the largest angle for depth in the shield beyond about 3 m.

Figs. 4 and 5 compare the results obtained with the preliminary simulations performed for case 2 and those with the final geometry setting (“selected bins” plus “shell per shell”) for 0–10°, 40–50°, 80–90° for 100 MeV and 0–10°, 40–50°, 80–90° and 130–140° for 250 MeV protons. This was done to check the effect of low-energy neutrons scat-

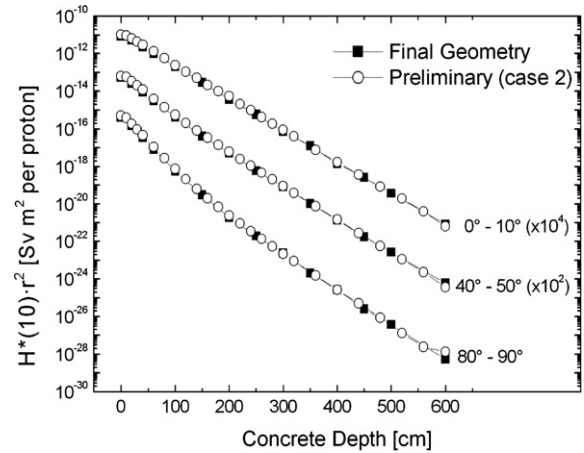


Fig. 4. Attenuation in ordinary concrete of the total dose equivalent produced by 100 MeV protons on a thick iron target: comparison of the results from preliminary simulations (case 2) with those achieved with the final geometry setting.

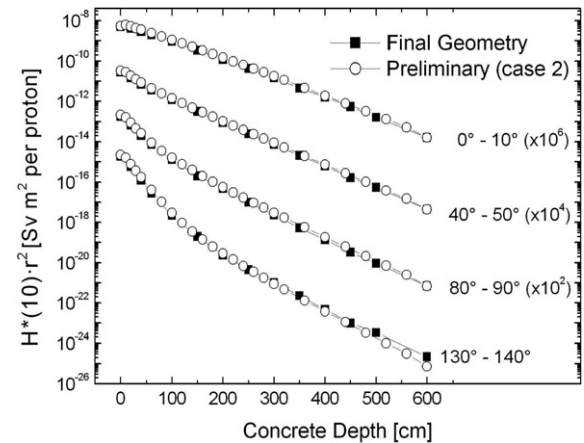


Fig. 5. Attenuation in ordinary concrete of the total dose equivalent produced by 250 MeV protons on a thick iron target: comparison of the results from preliminary simulations (case 2) with those achieved with the final geometry setting.

tered back and forth across a boundary estimator on the total dose. In almost all cases the preliminary data overestimate the final results by about 20%. As a general rule, the overestimate tends to increase with increasing angle and decreasing proton energy: the softer the spectrum, the larger the overestimate. The attenuation length varies by a few percent. As an example, Fig. 6 compares the neutron spectra from 250 MeV protons, in the 80–90° angular bin and at 400 cm depth in concrete for the preliminary case and for the final geometry setting. As expected, the main difference between the energy distributions is below a few MeV, because of neutrons scattered back and forth across a boundary-crossing estimator.

Fig. 7 compares the results obtained with the preliminary simulations performed for case 3 and the final results at 80–90° for 250 MeV protons in order to assess the “cross-talk” from the inner surface of the sphere. The two data sets agree within their statistical uncertainties,

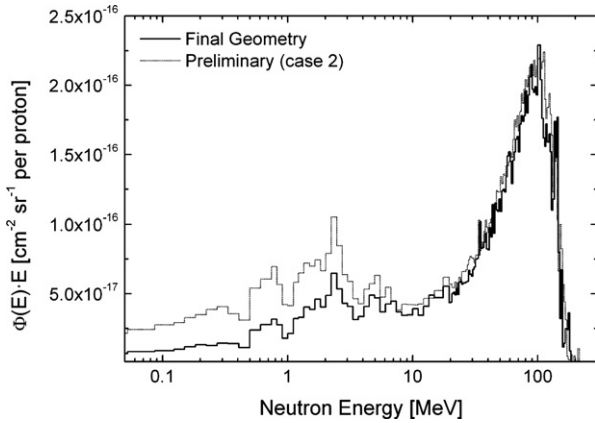


Fig. 6. Comparison of neutron spectra between the preliminary simulation (case 2) and the final geometry setting, scored after 400 cm of concrete in the 80–90° angular bin, for 250 MeV protons striking a thick iron target.

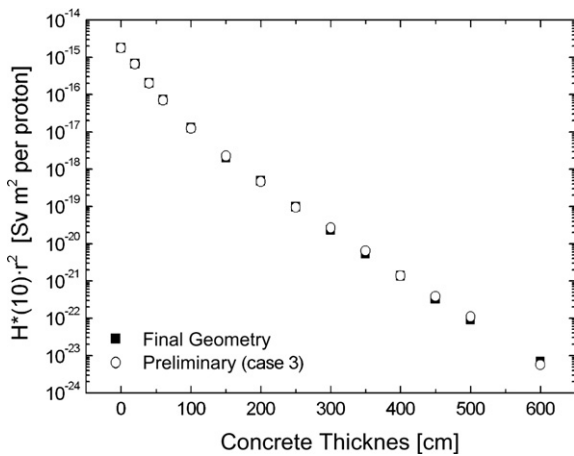


Fig. 7. Attenuation in ordinary concrete of the total dose equivalent produced by 250 MeV protons on a thick iron target: comparison of the results from preliminary simulations (case 3) with those achieved with the final geometry settings.

which are of the order of 2%. It is clear that this problem only concerns the first layers of the concrete shield, as it involves low-energy neutrons, whereas the dose at depth is mainly due to high energy neutrons. The fitting curves are practically identical within their statistical uncertainties, which are maximum 30% on the source term and 2.5% on the attenuation length.

A number of simulations were devoted to determine the target size which would ensure the most conservative combination between neutron yield and spectrum hardness. As a general rule, at a given proton energy, the larger is the transverse dimension of the target, the higher is the yield and the lower is the average energy of the distribution, as it is shown in Figs. 8 and 9 and in Table 2, which give the results for 250 MeV protons on targets of various dimensions. This is consistent with past results [12]. As the high energy neutron yield varies little with target size, the radius of the target was chosen to represent typical

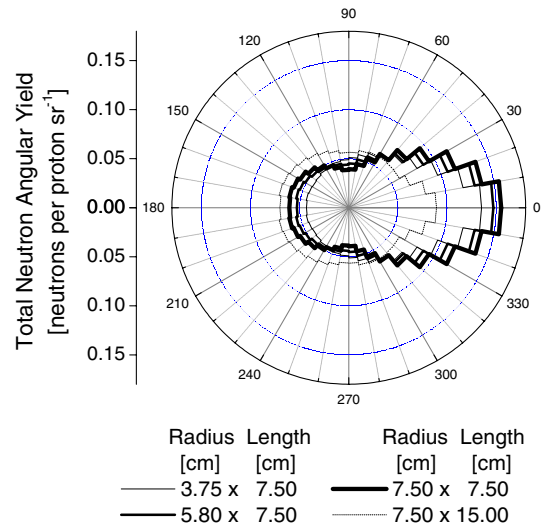


Fig. 8. Total neutron angular yield (neutrons per impinging proton per steradian) for four different target dimensions for 250 MeV protons.

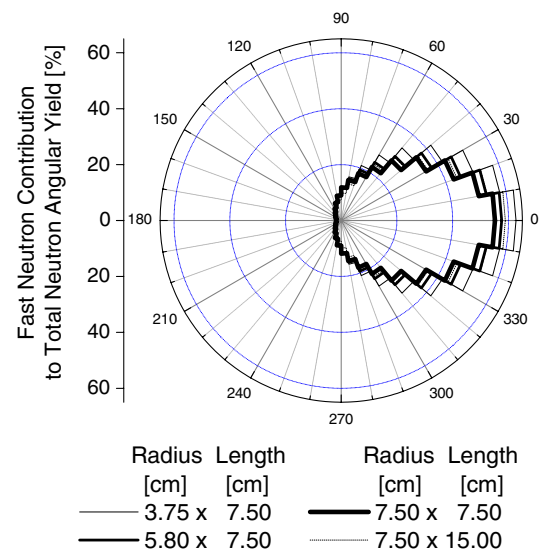


Fig. 9. Fast neutron contribution ( $E_n > 19.6$  MeV) to the total neutron angular yield for four different target dimensions for 250 MeV protons.

dimensions of accelerator components. Differences at low energy are of no relevance for shielding purposes. Table 3 lists the target dimensions used in the calculations (proton ranges in iron were taken from [13]). The neutron energy distributions from the four targets have the same shape and only differ in their absolute value (i.e. the total yield), due to small differences in both the neutron production and the self-absorption in the target.

To assess the effect of the target dimensions on neutron transport in concrete, Fig. 10 compares the results obtained with the preliminary simulations performed for case 5 with the final results for 250 MeV protons. The plot compares the attenuation of the total dose equivalent for secondary radiation produced by protons stopped in the “nominal” target used in the present work (5.8 cm in radius and

Table 2

Neutron yields (for neutrons with energy below and above 19.6 MeV, and total) and spectral average energies in the angular bins of interest, for 250 MeV protons striking iron targets of different longitudinal and transverse dimensions

Radius (cm) × Length (cm)	Neutrons per primary			$\langle E_n \rangle$ (MeV)			
	$E_n < 19.6$ MeV	$E_n > 19.6$ MeV	$n_{\text{tot}}$	0–10°	40–50°	80–90°	130–140°
3.75 × 7.50	0.567	0.148	0.715	73.6	25.9	8.1	3.9
5.80 × 7.50	0.586	0.140	0.726	67.7	22.9	8.1	3.6
7.50 × 7.50	0.596	0.136	0.732	64.7	21.3	8.1	3.5
7.50 × 15.00	0.671	0.111	0.782	70.3	23.5	6.9	3.2

The statistical uncertainties associated to the yield values are maximum 0.1% whereas those associated to the spectral average energies are maximum 0.5%, for all target dimensions.

Table 3

Target dimensions used in the final Monte Carlo simulations

$E_p$ (MeV)	Iron $\rho = 7.874 \text{ g cm}^{-3}$		
	Range (mm)	Radius (mm)	Thickness (mm)
100	14.45	10	20
150	29.17	15	30
200	47.65	25	50
250	69.30	58	75

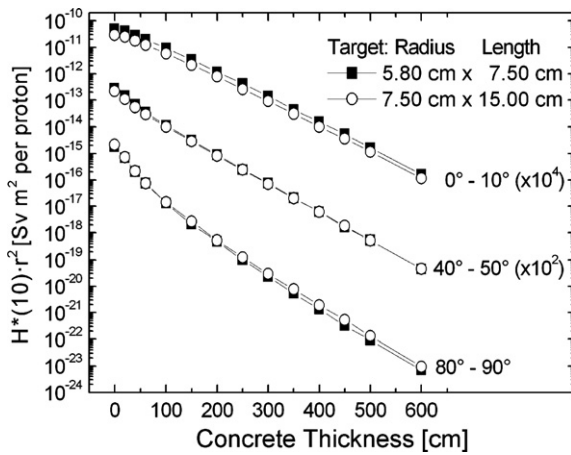


Fig. 10. Attenuation in ordinary concrete of the total dose equivalent produced by 250 MeV protons on two different thick iron targets: comparison of the results from preliminary simulations (case 5) with a thicker target with those achieved with the target used for the final calculations.

7.5 cm long) and a target thicker both in its transverse and longitudinal dimensions (7.5 cm × 15 cm). With respect to the nominal target, in the case of the thicker target the

Table 4

Comparison of source terms and attenuation lengths for concrete, for a 5.8 cm radius × 7.5 cm long iron target and for a 7.5 cm radius × 15 cm long iron target (preliminary simulation: case 5), for 250 MeV protons

Angular bin	Target dimensions: radius (cm) × length (cm)				$H^*(10)_{(b)}/H^*(10)_{(a)}$	$\lambda_{(b)}/\lambda_{(a)}$
	5.80 × 7.50 (a)		7.50 × 15.00 (b)			
	$H^*(10)$ (Sv m² per proton)	$\lambda$ (g cm⁻²)	$H^*(10)$ (Sv m² per proton)	$\lambda$ (g cm⁻²)		
0–10°	$(9.8 \pm 1.0) \times 10^{-15}$	$105.4 \pm 1.4$	$(5.9 \pm 0.5) \times 10^{-15}$	$106.9 \pm 1.1$	0.61	1.01
40–50°	$(1.2 \pm 0.1) \times 10^{-15}$	$93.5 \pm 0.5$	$(1.0 \pm 0.1) \times 10^{-15}$	$94.8 \pm 0.3$	0.84	1.01
80–90°	$(9.0 \pm 2.5) \times 10^{-17}$	$83.7 \pm 2.0$	$(1.0 \pm 0.1) \times 10^{-16}$	$85.1 \pm 1.0$	1.11	1.02

expected dose equivalent in the forward direction is about 40% lower at the shield surface (0 cm) and about 30% lower at 600 cm depth. In the 40–50° bin, the thicker target would reduce the dose by about 20% at 0 cm and by less than 3% from 250 cm depth inwards. In the 80–90° bin the situation is reversed: with the thicker target the dose equivalent is slightly overestimated, by less than 10% up to 100 cm depth in the shield, and by about 40% at 300 cm. Table 4 shows that the attenuation lengths are the same within their statistical uncertainties and the source terms deviate maximum by 40%. This comparison shows that the considered target dimensions do not affect the attenuation length and cause only slight deviations on the source term. The neutron spectrum and therefore the dose equivalent past the shield are not very sensitive to the target size (at least for the dimensions considered in this work).

Depending on the energy, angle of emission of the secondary radiation and actual geometry, in a real case of assessing radiation shielding of a given facility, some of the effects which in the simulations discussed in the next sections are excluded, may in fact be present. These specifically concern scattering within an extended barrier, room scattering and secondary radiation emitted backwards generated within the barrier. Therefore, as mentioned in the introduction, after a first estimate of the shield thickness through the data given in the present paper, a (partial) simulation of the facility in its real geometry may nonetheless be necessary.

### 3. Energy and angular distributions of source neutrons

The capability of FLUKA to correctly predict neutron energy distributions in a variety of conditions and energy ranges has been extensively benchmarked (see, for example,

[8,9]). A comparison of double differential distributions predicted by FLUKA at various angles at a proton energy of 256 MeV with experimental data [14] can be found in a previous paper [12], which also compares predictions made by FLUKA and LCS [15].

The double differential distributions of neutrons produced by protons with energy from 100 to 250 MeV impinging on a thick iron target, results of the present FLUKA simulations, are shown in Figs. 11–14 as lethargy plots. For all angles and proton energies, the statistical uncertainties are typically lower than 20% for all energy bins. The bins at the low and high energy tails of the distributions are affected by larger uncertainties. Since high energy neutrons are responsible for a large fraction of the dose equivalent beyond a thick shield, the associated uncertainties are crucial. Table 5 lists the threshold neutron energy above which the neutron fluence is affected by an uncertainty larger than 20%, the percent contribution to the neutron ambient dose equivalent  $H^*(10)_n$  after a 300 cm thick concrete shield from these neutrons, and the ratio

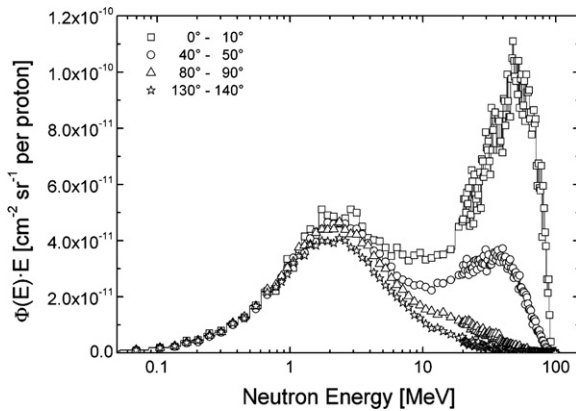


Fig. 11. Double differential distributions of neutrons from 100 MeV protons impinging on a thick iron target, calculated with the FLUKA code.

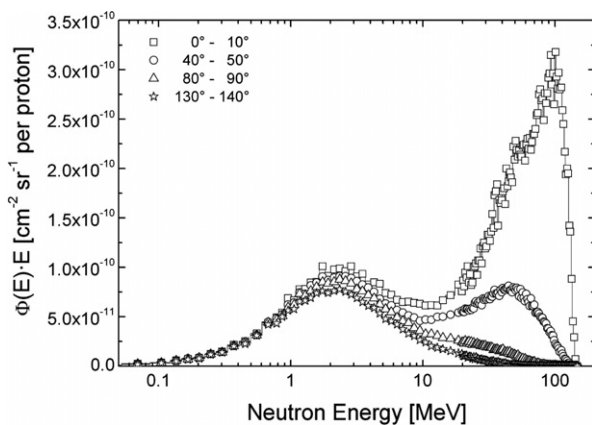


Fig. 12. Double differential distributions of neutrons from 150 MeV protons impinging on a thick iron target, calculated with the FLUKA code.

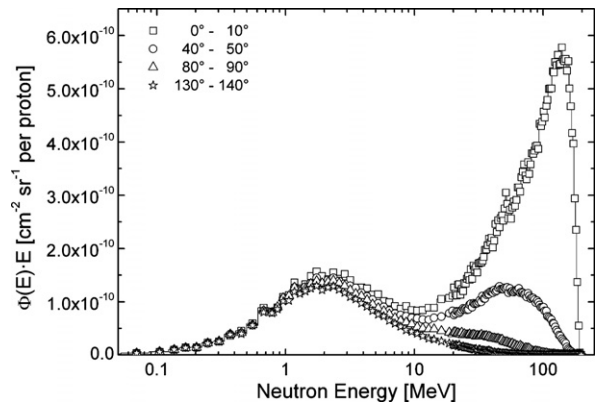


Fig. 13. Double differential distributions of neutrons from 200 MeV protons impinging on a thick iron target, calculated with the FLUKA code.

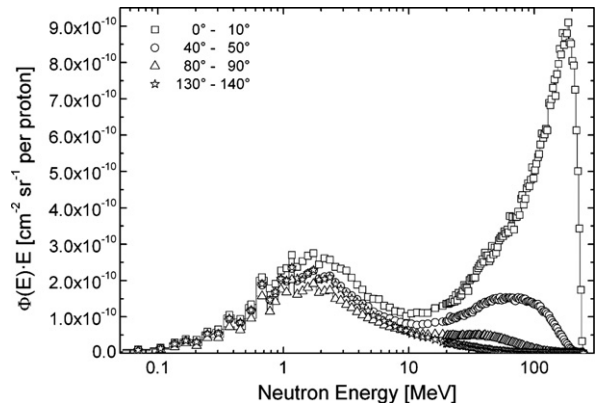


Fig. 14. Double differential distributions of neutrons from 250 MeV protons impinging on a thick iron target, calculated with the FLUKA code.

of total  $H^*(10)$  past the shield to the corresponding source value. As an example, for  $E_p = 100$  MeV and  $130\text{--}140^\circ$  angular bin, above 30 MeV the neutron energy distribution is affected by an uncertainty larger than 20%, and these neutrons contribute almost 30% of  $H^*(10)_n$  past the shield. In addition, high energy neutrons not only drive the attenuation through the shield, but also generate all equilibrium low energy neutrons. Therefore, their impact on  $H^*(10)$  is larger than their “local” percentage contribution given in the above discussion. One has therefore to be much careful as a poorly sampled high energy tail might have a substantial impact on the results. Nonetheless, the attenuation provided by a thick shield is normally so large (a factor of more than  $10^8$  in the present example) that a fairly high uncertainty may be accepted in a practical situation in which the dose equivalent rate would be anyhow very low (e.g.  $5 \text{ nSv h}^{-1}$  outside the shield for a source dose rate of  $1 \text{ Sv h}^{-1}$ ).

The energy distributions in Figs. 11–14 represent the main radiation source for the shielding calculations. They are typically characterised by two peaks, a high energy peak and an evaporation peak. One notices the increasing

Table 5

Threshold neutron energy above which the fluence of the source neutrons is affected by a statistical uncertainty of more than 20%, percent contribution to neutron ambient dose equivalent  $H^*(10)_n$  past a 300 cm thick concrete shield from these neutrons, and ratio of total  $H^*(10)$  past 300 cm concrete to the corresponding source term value at the inner surface of the shield (0 cm)

Proton energy (MeV)	Angular bin	Neutron energy (MeV)	Percent fraction to $H^*(10)_n$ (%)	$H^*(10)$ at 300 cm/ $H^*(10)$ at 0 cm
100	0–10°	90	<0.1	$8.7 \times 10^{-6}$
	40–50°	80	1.2	$1.4 \times 10^{-6}$
	80–90°	50	20.5	$5.8 \times 10^{-8}$
	130–140°	30	28.3	$5.8 \times 10^{-9}$
150	0–10°	140	<0.1	$2.7 \times 10^{-5}$
	40–50°	130	0.1	$2.3 \times 10^{-5}$
	80–90°	75	11.7	$6.9 \times 10^{-7}$
	130–140°	50	24.1	$3.8 \times 10^{-8}$
200	0–10°	190	<0.1	$1.4 \times 10^{-3}$
	40–50°	175	0.1	$1.2 \times 10^{-4}$
	80–90°	110	4.1	$3.5 \times 10^{-6}$
	130–140°	60	18.3	$9.6 \times 10^{-8}$
250	0–10°	240	<0.1	$2.8 \times 10^{-3}$
	40–50°	220	<0.1	$2.7 \times 10^{-4}$
	80–90°	150	0.9	$1.3 \times 10^{-5}$
	130–140°	80	16.2	$5.3 \times 10^{-7}$

Table 6

Neutron yield and average neutron energy at the four emission angles for 100–250 MeV protons on a thick iron target

Proton energy (MeV)	Neutron yield (neutrons per proton)			Average neutron energy $\langle E_n \rangle$ (MeV)			
	$E_n < 19.6$ MeV	$E_n > 19.6$ MeV	$n_{\text{tot}}$	0–10°	40–50°	80–90°	130–140°
100	0.118	0.017	0.135	22.58	12.06	4.96	3.56
150	0.233	0.051	0.284	40.41	17.26	6.29	3.93
200	0.381	0.096	0.477	57.73	22.03	7.38	3.98
250	0.586	0.140	0.726	67.72	22.90	8.09	3.62

The statistical uncertainties associated to the yield values are less than 0.25% (the worst case being at 100 MeV) whereas those associated to the spectral average energies are 1% maximum.

ratio between the two peaks with increasing proton energy, particularly evident in the forward direction but also noticeable at 40–50°. At 250 MeV one also sees that in the evaporation zone the distributions at 80–90° and 130–140° reverse: this is because, unlike for the simulations at the other energies, the target used at 250 MeV is not a right cylinder but it is larger in diameter than in length (11.6 cm in diameter and 7.5 cm thick).

Table 6 lists the neutron yields integrated over the entire solid angle for the various proton energies, along with the average energy of the distributions at the various emission angles.

#### 4. Shielding parameters

In general, the attenuation through a thick shield of the total ambient dose equivalent is fitted with the classical two-parameter formula (see, for example, [6]):

$$H(E_p, \theta, d/\lambda) = \frac{H_0(E_p, \theta)}{r^2} \exp \left[ -\frac{d}{\lambda(\theta)g(\alpha)} \right], \quad (1)$$

where  $H$  is the ambient dose equivalent beyond the shield,  $E_p$  is the proton energy,  $r$  is the distance between the radiation source (the target stopping the protons) and the scoring position,  $\theta$  is the angle between the direction  $\vec{r}$  and the

beam axis,  $H_0$  is the source term,  $d$  is the shield thickness,  $\lambda(\theta)$  is the attenuation length for the given shielding material at emission angle, and  $\alpha$  is the angle between the direction  $\vec{r}$  and the normal to the shield surface. The function  $g(\alpha) = 1$  for the spherical geometry used in the present simulations and  $g(\alpha) = \cos \alpha$  in all other cases. This is the expression used in the present work to fit the data in the forward direction (after the build-up region extending to a depth of about 100 cm, after which the attenuation becomes exponential).

It has been shown before (and explained in the next section) that in certain cases the attenuation of the dose equivalent is better expressed by a double-exponential [16,17]

$$H(E_p, \theta, d/\lambda) = \frac{H_1(E_p, \theta)}{r^2} \exp \left[ -\frac{d}{\lambda_1(\theta)g(\alpha)} \right] + \frac{H_2(E_p, \theta)}{r^2} \exp \left[ -\frac{d}{\lambda_2(\theta)g(\alpha)} \right], \quad (2)$$

where  $H_1$ ,  $\lambda_1(\theta)$  and  $H_2$ ,  $\lambda_2(\theta)$  are the source terms and the attenuation lengths for the shallow-depth and large-depth (deep penetration) exponential functions, respectively. The second term of expression (2) describes the attenuation for a shield thicker than about 100 cm and obviously cannot be applied for a thinner shield, because it would lead to an underestimate of the ambient dose equivalent.

In practice, expression (2) includes expression (1) by setting  $H_0 = H_2$ ,  $\lambda(\theta) = \lambda_2(\theta)$  and setting the first term to zero (i.e.  $H_1 = \lambda_1(\theta) = 0$ ). As shown in the next section, a double-exponential attenuation is characteristic of the attenuation curves in the 40–50°, 80–90° and 130–140° angular bins.

## 5. Shielding data for concrete

The attenuation of the total dose equivalent in ordinary concrete at the four emission angles are plotted in Figs. 15–18 for 100, 150, 200 and 250 MeV protons impinging on a thick iron target. The statistical uncertainties on the data points is less than 6% at 250 MeV and less than 10% at 100 MeV, the maximum always being at the largest depths at the backward angles. For the sake of clarity only the fit on the second exponential in expression (2) is shown. The

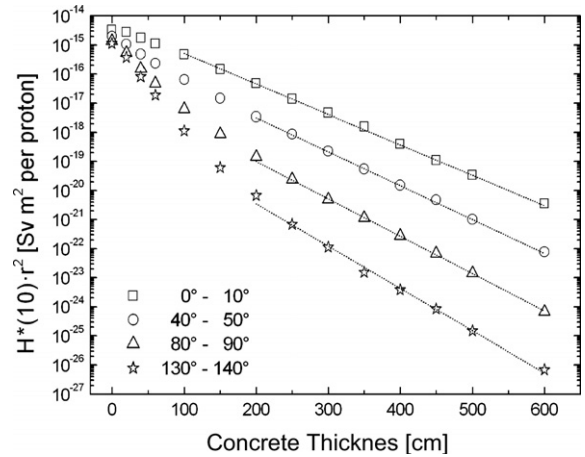


Fig. 17. Attenuation of total dose equivalent in ordinary concrete for 200 MeV protons impinging on a thick iron target. Only the fit on the second exponential is shown. The statistical uncertainties of each data point are smaller than the size of the symbol.

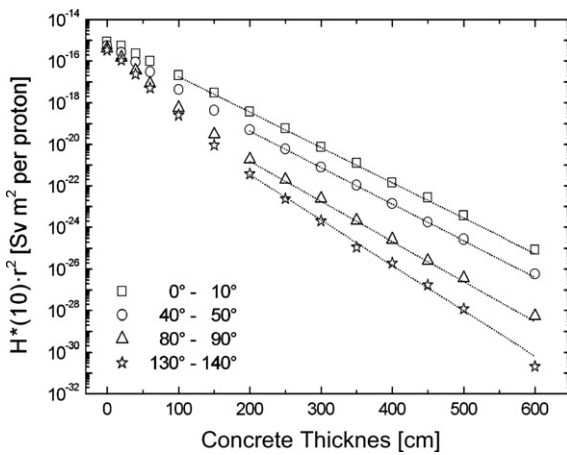


Fig. 15. Attenuation of total dose equivalent in ordinary concrete for 100 MeV protons impinging on a thick iron target. Only the fit on the second exponential is shown. The statistical uncertainties of each data point are smaller than the size of the symbol.

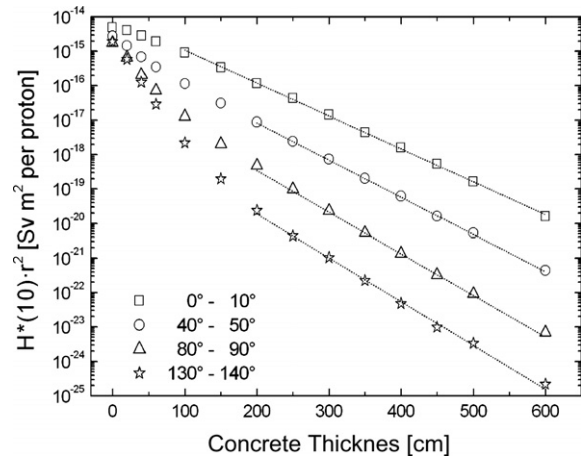


Fig. 18. Attenuation of total dose equivalent in ordinary concrete for 250 MeV protons impinging on a thick iron target. Only the fit on the second exponential is shown. The statistical uncertainties of each data point are smaller than the size of the symbol.

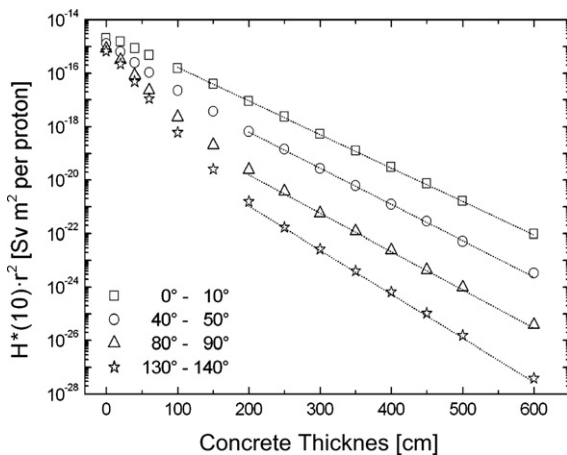


Fig. 16. Attenuation of total dose equivalent in ordinary concrete for 150 MeV protons impinging on a thick iron target. Only the fit on the second exponential is shown. The statistical uncertainties of each data point are smaller than the size of the symbol.

resulting source terms  $H_0$  (Sv m<sup>2</sup> per proton) and attenuation lengths  $\lambda$  (g cm<sup>-2</sup>) are listed in Table 7.

At small depths and at the forward angle a dose build-up region is visible, particularly at the highest energies. Moving towards larger angles this situation is reversed, as the low energy component starts to dominate and a fast attenuation region appears at small thicknesses. This is because the neutron energy distributions vary with depth in concrete. The spectrum hardens until a depth of about 100 cm, after which it reaches equilibrium. As an example, Fig. 19 shows the normalised neutron energy distributions (areas are normalized to unity in order to show the variations in the spectral shape) in the transverse direction from 250 MeV protons at the surface of a concrete shield and at 20, 40, 60, 100 and 600 cm depth. The lower energy component of the spectrum is attenuated mostly up to a depth in the shield of about 100 cm with a short attenuation

Table 7  
Attenuation of the total dose equivalent in ordinary concrete for 100–250 MeV protons impinging on a thick iron target

	Angular bin	First exponential		Second exponential	
		$H_1(10)$ (Sv m <sup>2</sup> per proton)	$\lambda_1(\theta)$ (g cm <sup>-2</sup> )	$H_2(10)$ (Sv m <sup>2</sup> per proton)	$\lambda_2(\theta)$ (g cm <sup>-2</sup> )
100 MeV	0–10°	–	–	$(8.9 \pm 0.4) \times 10^{-16}$	$59.7 \pm 0.2$
	40–50°	$(5.9 \pm 1.3) \times 10^{-16}$	$47.5 \pm 2.7$	$(1.5 \pm 0.1) \times 10^{-16}$	$57.2 \pm 0.3$
	80–90°	$(5.3 \pm 0.8) \times 10^{-16}$	$33.7 \pm 1.2$	$(1.1 \pm 0.3) \times 10^{-17}$	$52.6 \pm 0.7$
	130–140°	$(4.7 \pm 0.4) \times 10^{-16}$	$30.7 \pm 0.5$	$(8.0 \pm 5.1) \times 10^{-18}$	$46.1 \pm 2.8$
150 MeV	0–10°	–	–	$(3.0 \pm 0.2) \times 10^{-15}$	$80.4 \pm 0.5$
	40–50°	$(1.2 \pm 0.2) \times 10^{-15}$	$57.8 \pm 3.4$	$(3.3 \pm 0.8) \times 10^{-16}$	$74.3 \pm 1.4$
	80–90°	$(10.0 \pm 2.2) \times 10^{-16}$	$37.4 \pm 2.7$	$(1.2 \pm 0.3) \times 10^{-17}$	$70.8 \pm 1.3$
	130–140°	$(7.8 \pm 2.0) \times 10^{-16}$	$32.1 \pm 1.5$	$(2.1 \pm 0.6) \times 10^{-18}$	$61.8 \pm 1.1$
200 MeV	0–10°	–	–	$(5.6 \pm 0.4) \times 10^{-15}$	$96.6 \pm 0.8$
	40–50°	$(1.9 \pm 0.3) \times 10^{-15}$	$68.3 \pm 5.9$	$(6.8 \pm 0.5) \times 10^{-16}$	$86.4 \pm 0.5$
	80–90°	$(1.3 \pm 0.4) \times 10^{-15}$	$43.8 \pm 4.4$	$(3.7 \pm 0.8) \times 10^{-17}$	$78.3 \pm 1.3$
	130–140°	$(1.3 \pm 0.3) \times 10^{-15}$	$32.8 \pm 1.6$	$(2.8 \pm 2.4) \times 10^{-18}$	$70.0 \pm 4.1$
250 MeV	0–10°	–	–	$(9.8 \pm 1.0) \times 10^{-15}$	$105.4 \pm 1.4$
	40–50°	$(2.3 \pm 0.5) \times 10^{-15}$	$77.0 \pm 7.9$	$(1.2 \pm 0.1) \times 10^{-15}$	$93.5 \pm 0.5$
	80–90°	$(1.4 \pm 0.4) \times 10^{-15}$	$49.7 \pm 5.7$	$(9.0 \pm 2.5) \times 10^{-17}$	$83.7 \pm 2.0$
	130–140°	$(1.9 \pm 0.6) \times 10^{-15}$	$34.4 \pm 3.4$	$(6.5 \pm 2.6) \times 10^{-18}$	$79.1 \pm 3.4$

Source terms  $H_1$  and  $H_2$  (Sv m<sup>2</sup> per proton) and attenuation lengths  $\lambda_1$  and  $\lambda_2$  (g cm<sup>-2</sup>) resulting from the fits shown in Figs. 15–18.

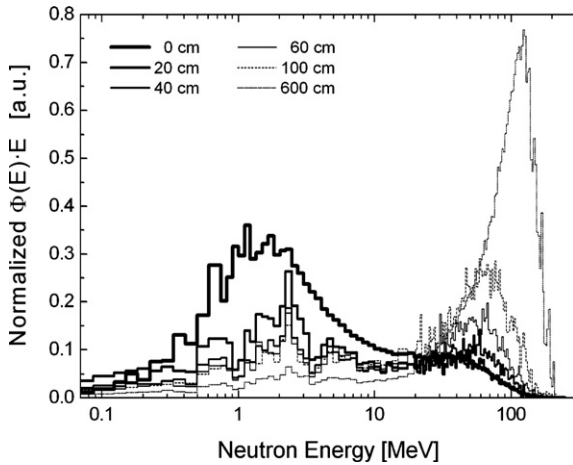


Fig. 19. Neutron energy distributions (normalized to 1) in the transverse direction generated by 250 MeV protons, at the surface of a concrete shield and at 20, 40, 60, 100 and 600 cm depth.

length – the first term in expression (2) – giving rise to a less intense but harder and more penetrating spectral distribution, which is characterised by a longer attenuation length – the second term in expression (2).

For each proton energy and each angular bin,  $H_0$  and  $\lambda$  in Table 7 were obtained by averaging the results of several, independent exponential fits. Each  $i$ -th fitting curve providing the corresponding  $i$ -th ( $H_0, \lambda$ ) pair is the 2-parameter curve given above, obtained with different extremes of the data range to be fitted. This was done in order to smooth the dependence of the attenuation length and the associated uncertainty on the statistical fluctuations of the simulation data, and to appreciate the dependence of the value of the source term on the corresponding value of the attenuation length. For the forward direction expression (1) was used, taking into account data points between 100 cm and 600 cm. For the other directions the data were fitted with two independent exponentials (rather than with

the single 4-parameter fit of expression (2) as done in a previous work [16]), taking into account data points between 20 cm and 150 cm for the first exponential and data points between 200 cm and 600 cm for the second exponential. For the forward direction the associated uncertainties are less than 10% on both the source terms and the attenuation lengths, whereas for all other angular bins the uncertainties on the attenuation length are below 15%, whilst for the source term they can reach 85%. This is because the dose is proportional to the source term and depends exponentially on the attenuation length. Thus for a given dose past the shield, a small variation of the attenuation length leads to a large variation on the source term. Including in the fit for the second exponential data at shallower depths (between 200 and 350 cm), generally  $\lambda$  tends to increase and  $H_0$  to decrease.

The variations of the parameters  $H_0$  and  $\lambda$  with proton energy and emission angle are shown in Figs. 20–23 for the deep penetration term (thick shield) and in Figs. 24–27 for the shallow penetration term (thin shield). In general, data in the backward direction are affected by a larger statistical uncertainty with respect to the other angular bins.

The values of source term and attenuation length for deep penetration in Figs. 20–23 were fitted as a function of proton energy  $E_p$  and emission angle  $\theta$  according to the following expressions:

$$H_{0(E_p)} = P_1 \cdot \exp\left(\frac{E_p}{P_2}\right), \quad (3)$$

$$\lambda_{(E_p)} = \frac{A}{1 + \exp\left[\frac{\ln(P_3) - \ln(E_p)}{P_4}\right]} + B, \quad (4)$$

$$H_{0(\theta)} = P_5 \cdot \exp\left(-\frac{\theta}{P_6}\right), \quad (5)$$

$$\lambda_{(\theta)} = P_7 - P_8 \cdot \theta. \quad (6)$$

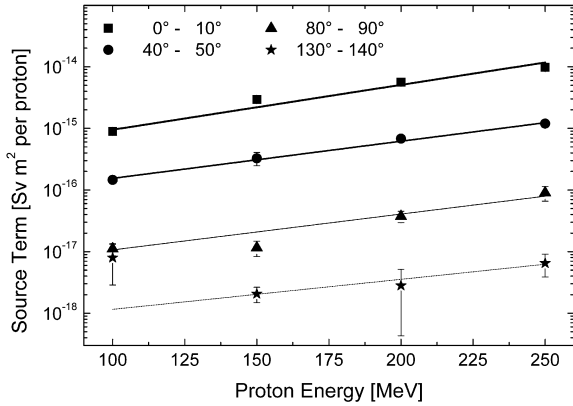


Fig. 20. Source term (second exponential – deep penetration) versus primary proton energy at emission angles of 0–10°, 40–50°, 80–90° and 130–140° for neutrons produced by 100–250 MeV protons impinging on a thick iron target. The fits are according to expression (3).

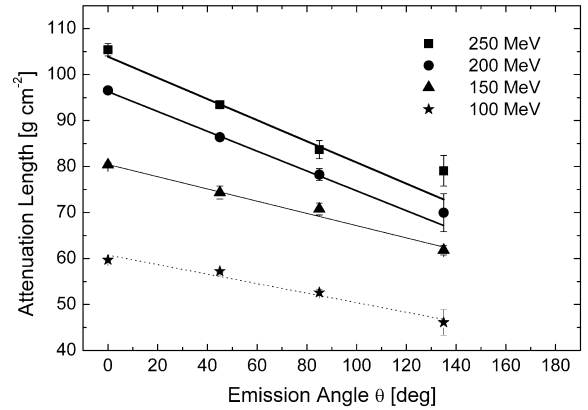


Fig. 23. Attenuation length in concrete (second exponential – deep penetration) versus emission angle for neutrons produced by 100–250 MeV protons impinging on a thick iron target. The fits are according to expression (6).

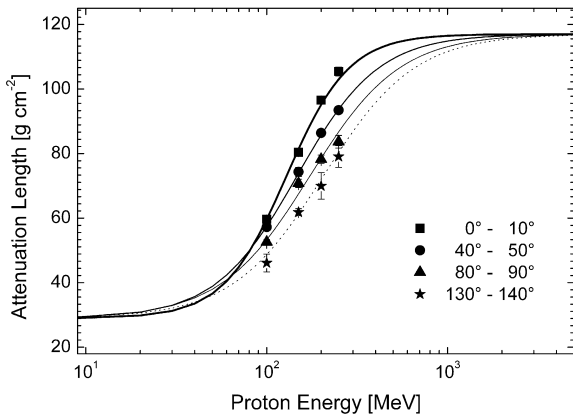


Fig. 21. Attenuation length in concrete (second exponential – deep penetration) versus primary proton energy at emission angles of 0–10°, 40–50°, 80–90° and 130–140° for neutrons produced by 100–250 MeV protons impinging on a thick iron target. The fits are according to expression (4).

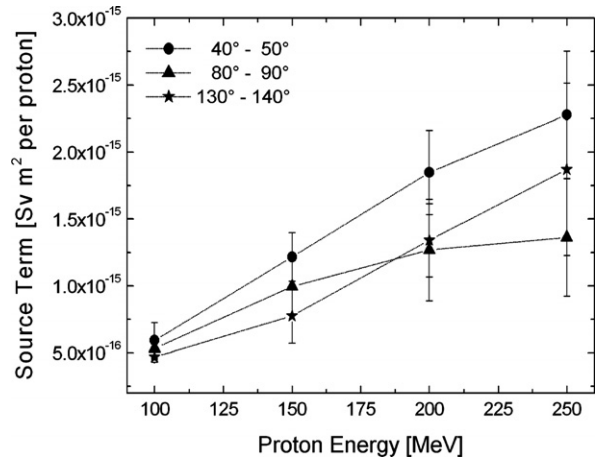


Fig. 24. Source term (first exponential – thin shield) versus primary proton energy at emission angles of 40–50°, 80–90° and 130–140° for neutrons produced by 100–250 MeV protons impinging on a thick iron target. The lines are only to guide the eye.

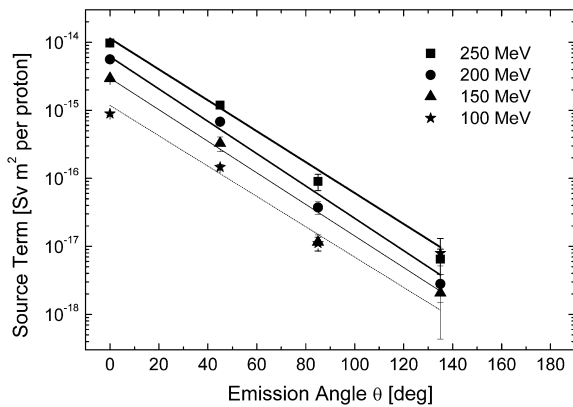


Fig. 22. Source term (second exponential – deep penetration) versus emission angle for neutrons produced by 100–250 MeV protons impinging on a thick iron target. The fits are according to expression (5).

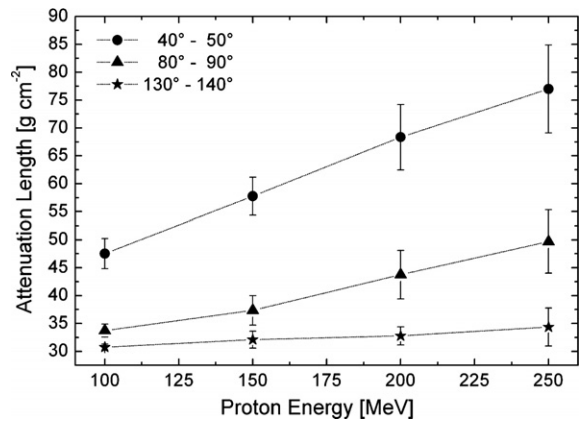


Fig. 25. Attenuation length in concrete (first exponential – thin shield) versus primary proton energy at emission angles of 40–50°, 80–90° and 130–140° for neutrons produced by 100–250 MeV protons impinging on a thick iron target. The lines are only to guide the eye.

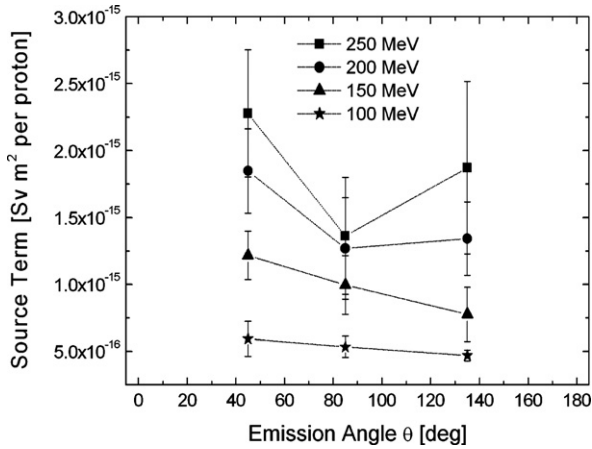


Fig. 26. Source term (first exponential – thin shield) versus emission angle for neutrons produced by 100–250 MeV protons impinging on a thick iron target. The lines are only to guide the eye.

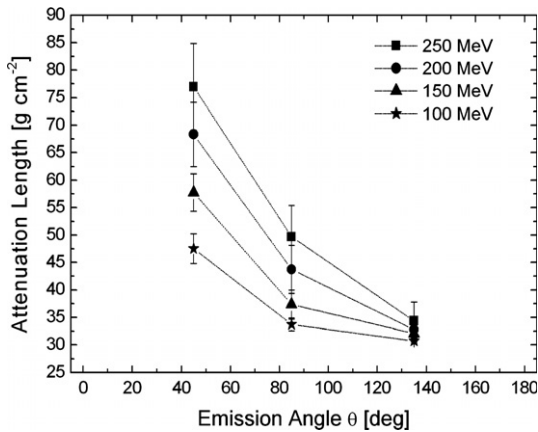


Fig. 27. Attenuation length in concrete (first exponential – thin shield) versus emission angle for neutrons produced by 100–250 MeV protons impinging on a thick iron target. The lines are only to guide the eye.

Table 8 gives the parameters of the fits shown in Figs. 20–23. The variation of the source term versus both energy and

emission angle is fairly well described by an exponential function, whilst the attenuation length varies approximately linearly with angle. A more complex mathematical function was used to fit the attenuation length versus proton energy, in order to follow its well-known behaviour (see, for example, [6], p. 224): a low-energy limit of about  $29 \text{ g cm}^{-2}$ , a high-energy limit around  $117 \text{ g cm}^{-2}$ , and a transition zone in-between. A and B in expression (4) are set in order to respect such limits:  $A = 88 \text{ g cm}^{-2}$  and  $B = 29 \text{ g cm}^{-2}$ . The above expressions can be used to interpolate the shielding parameters in the 100–250 MeV energy range and for emission angles from forward to about  $150^\circ$ , and with some caution to extrapolate slightly outside this range. Expression (4) can to a certain extent be used to extrapolate  $\lambda$ -values outside the 100–250 MeV energy range.

The total ambient dose equivalent past a concrete shield is mainly due to neutrons, but photons and protons cannot sometimes be completely neglected. The non-neutron part of the dose equivalent is usually limited to a few percent, except in the backward direction where photons contribute more than 10% and up to 35% to the total dose for a shield thickness of one to two meters. Generally speaking, the non-neutron contribution decreases with increasing energy of the primary proton and increases with increasing angle: in particular, the contribution from secondary protons is maximum in the forward direction (because of protons generated in the intranuclear cascade) and decreases with angle, whereas the electromagnetic contribution (possibly dominated by prompt gamma rays) moves in the opposite direction. The percent contribution of neutrons, photons, protons and electrons to the total dose equivalent past a concrete shield of increasing thickness is shown in Figs. 28–31 for 100 and 250 MeV protons for the forward and the backward directions. Table 9 lists the maximum contribution of protons, photons and electrons to total dose for the various angular bins and proton energies.

Table 8

Fitting parameters of source term and attenuation length as a function of proton energy Panel 1 and as a function of emission angle Panel 2

Angular bin	Source term		Attenuation length	
	$P_1$ (Sv m <sup>2</sup> per proton)	$P_2$ (MeV)	$P_3$ (MeV)	$P_4$ (a.u.)
<i>Panel 1</i>				
0–10°	$(1.8 \pm 0.2) \times 10^{-16}$	$59.7 \pm 2.2$	$128.5 \pm 0.6$	$0.40 \pm 0.01$
40–50°	$(3.9 \pm 0.6) \times 10^{-17}$	$72.1 \pm 3.5$	$146.8 \pm 0.9$	$0.52 \pm 0.01$
80–90°	$(2.8 \pm 1.3) \times 10^{-18}$	$74.7 \pm 13.6$	$173.0 \pm 3.4$	$0.57 \pm 0.03$
130–140°	$(3.8 \pm 3.6) \times 10^{-19}$	$89.0 \pm 40.6$	$205.5 \pm 9.7$	$0.58 \pm 0.08$
$E_p$ (MeV)	$P_5$ (Sv m <sup>2</sup> per proton)	$P_6$ (deg)	$P_7$ (g cm <sup>-2</sup> )	$P_8$ (g cm <sup>-2</sup> deg <sup>-1</sup> )
<i>Panel 2</i>				
100	$(1.2 \pm 0.1) \times 10^{-15}$	$19.5 \pm 0.7$	$61.1 \pm 0.9$	$0.11 \pm 0.01$
150	$(3.9 \pm 0.3) \times 10^{-15}$	$17.9 \pm 0.7$	$81.1 \pm 0.5$	$0.14 \pm 0.01$
200	$(8.1 \pm 0.6) \times 10^{-15}$	$17 \pm 0.5$	$97.2 \pm 0.7$	$0.23 \pm 0.02$
250	$(1.4 \pm 0.1) \times 10^{-14}$	$17.9 \pm 0.6$	$106.2 \pm 0.3$	$0.28 \pm 0.03$

See text, expressions (3)–(6). The comparatively larger uncertainties for P1 and P2 at 80–90° and 130–140° are easy to understand from the fits in Fig. 20.

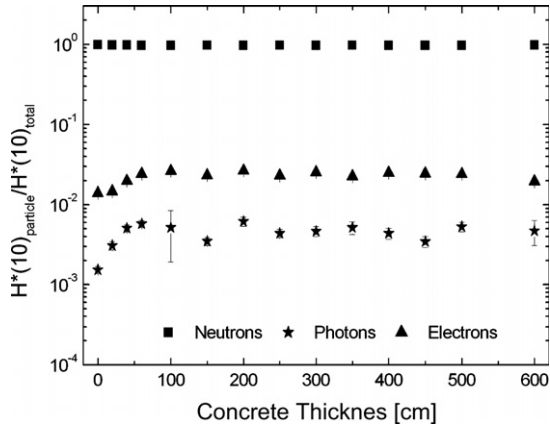


Fig. 28. Percent contribution of the various particles to the total dose equivalent past a concrete shield of increasing thickness. Simulation results are for secondary radiation in the forward direction (0–10° bin) from 100 MeV protons on a thick iron target. Protons are not shown as their contribution is below 0.1%.

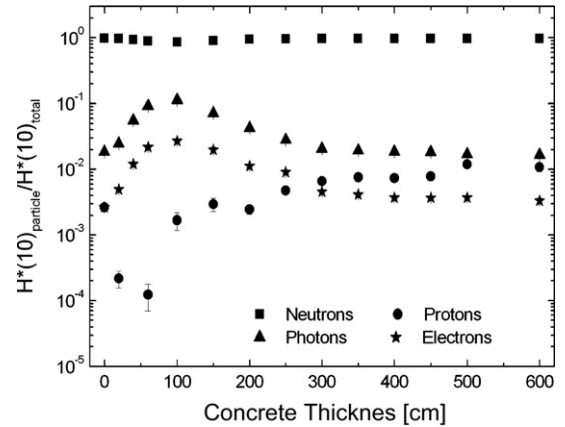


Fig. 31. Percent contribution of the various particles to the total dose equivalent past a concrete shield of increasing thickness. Simulation results are for secondary radiation in the backward direction (130–140° bin) from 250 MeV protons on a thick iron target.

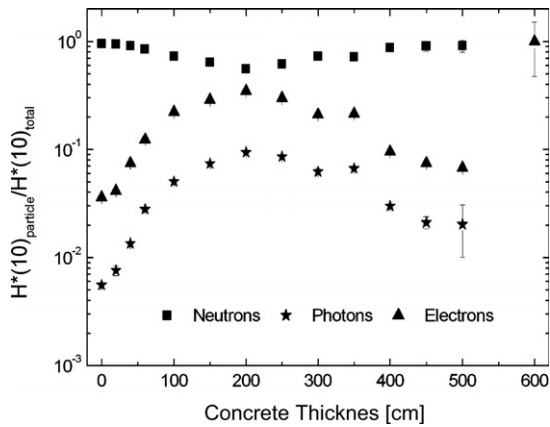


Fig. 29. Percent contribution of the various particles to the total dose equivalent past a concrete shield of increasing thickness. Simulation results are for secondary radiation in the backward direction (130–140° bin) from 100 MeV protons on a thick iron target. Protons are not shown as their contribution is below 0.1%.

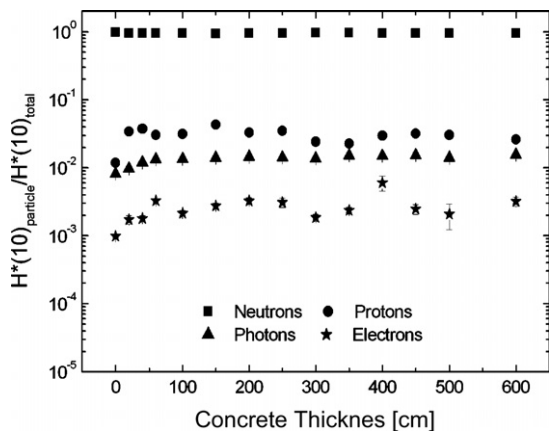


Fig. 30. Percent contribution of the various particles to the total dose equivalent past a concrete shield of increasing thickness. Simulation results are for secondary radiation in the forward direction (0–10° bin) from 250 MeV protons on a thick iron target.

Table 9

Maximum percent contribution of protons, photons and electrons to the total dose

Proton energy (MeV)	Angular Bin	Protons (%)	Photons (%)	Electrons (%)
100	0–10°	0.16	2.66	0.62
	40–50°	0.10	4.04	1.93
	80–90°	<0.10	13.08	2.99
	130–140°	<0.10	34.69	9.45
150	0–10°	2.12	1.97	0.56
	40–50°	0.48	2.76	0.68
	80–90°	0.67	7.26	1.89
	130–140°	0.30	19.58	4.63
200	0–10°	2.91	1.61	0.67
	40–50°	4.86	2.26	0.54
	80–90°	1.12	5.06	1.06
	130–140°	0.45	14.79	3.34
250	0–10°	4.33	1.56	0.60
	40–50°	2.45	2.04	0.47
	80–90°	1.27	4.13	0.82
	130–140°	1.19	11.30	2.70

Data are not necessarily at the same concrete thickness (see Figs. 28–31).

## 6. Comparison with literature data

The values of  $H_0$  and  $\lambda$  obtained in the previous section were compared with calculated (either by Monte Carlo simulations or analytically) and experimental data available in the literature [18,19,21,23,26,27,29–31,34]. Only data for angular bins comparable to those of the present work were taken from the quoted references for the comparison. The results of this extensive evaluation, performed for proton energies up to 400 MeV, are summarised in Tables 10(a), 10(b), 10(c).

### 6.1. Comparison with measurements (Table 10(a))

Siebers et al. [18] report both experimental results and Monte Carlo simulations of the experimental set-up. The comparison is made here only with the measured data,

Table 10(a)  
Comparison of source terms and attenuation lengths in concrete calculated in the present work with literature results (experimental data)

References	$E_p$ (MeV)		Emission angle		Source term (Sv m <sup>2</sup> per proton)		Attenuation length (g cm <sup>-2</sup> )	
	Literature data	Present work	Literature data	Present work	Literature data	Present work	Literature data	Present work
[18]	230	230 <sup>a</sup>	0°	0–10°	$(7.8 \pm 0.5) \times 10^{-15}$	$8.40 \times 10^{-15}$	$89.1 \pm 1.8$	100.4
			45°	40–50°	$(2.2 \pm 0.5) \times 10^{-15}$	$9.40 \times 10^{-16}$	$73 \pm 6$	91
			90°	80–90°	$(7.6 \pm 0.7) \times 10^{-16}$	$6.10 \times 10^{-17}$	$51.9 \pm 1.5$	83.8
[21]*	200	200	0°	0–10°	$(1.6 \pm 0.1) \times 10^{-15}$	$(5.6 \pm 0.4) \times 10^{-15}$	$90.0 \pm 3.0$	$96.6 \pm 0.8$
			22.5°	20–30° <sup>a</sup>	$(1.2 \pm 0.1) \times 10^{-15}$	$1.86 \times 10^{-15}$	$96.0 \pm 3.0$	91.4
			45°	40–50°	$(0.9 \pm 0.1) \times 10^{-15}$	$(6.8 \pm 0.5) \times 10^{-16}$	$100.0 \pm 23.0$	$86.4 \pm 0.5$
			67.5°	60–70° <sup>a</sup>	$(6.7 \pm 1.0) \times 10^{-16}$	$1.80 \times 10^{-16}$	$82.0 \pm 13.0$	82.2
			90°	80–90°	$(8.9 \pm 0.4) \times 10^{-16}$	$(3.7 \pm 0.8) \times 10^{-17}$	$68.0 \pm 6.0$	$78.3 \pm 1.3$

All targets are thick iron targets except <sup>a</sup>thick aluminium.

<sup>a</sup> Interpolated/extrapolated data were obtained from Eqs. (3)–(6) (see text, Section 5).

because the results of the simulations are identical to those of [19] (the same situation has been simulated with the same LCS code). The only discrepancy between the two papers is on the source terms, which in [18] are the double of those of [19] simply because the fluence-to-dose conversion coefficients have been doubled. Measurements were performed with 230 MeV protons at the Fermi National Accelerator Laboratory (Batavia, Illinois) with the proton synchrotron now installed at the Loma Linda University Medical Center (California). The concrete composition is substantially different from that of the present work (in particular, their concrete has a factor of 2 more H and a factor of 6 less C than that of the present simulations, and their density is  $1.88 \text{ g cm}^{-3}$  versus  $2.31 \text{ g cm}^{-3}$ ) which may explain the large difference in the attenuation lengths. The largest discrepancy is at 80–90°, where the attenuation lengths differ by about 40% and the source terms by around one order of magnitude. The dose equivalent values of [18] were derived from measurements of lineal energy spectra ([20]) inside cavities in the shield.

Measurements outside a concrete shield of increasing thickness at different angles were performed at the Centre de Protonthérapie d'Orsay with 200 MeV protons on a thick aluminum target [21]. Discrepancies with the present simulations are clearly visible both in attenuation lengths and source terms. Part of these discrepancies may be due to the concrete composition, which is not given in the paper. The dependence of the attenuation length on emission angle in [21] is a little striking because at 22.5° the attenuation length is about 5% larger than at 0°, and at 45° it is about 10% larger than at 0°. This effect would imply a spectrum hardening with increasing emission angle up to 45°. Moreover the attenuation lengths at 45° and 67.5° are affected by quite large uncertainties, which can in turn also affect the corresponding source terms and related uncertainties.

Finally, [22] discusses dose rate measurements performed at PSI (Switzerland) outside a concrete shield of increasing thickness (0.5 to 3 m in steps of 0.5 m) with 250 MeV protons stopped in a thick copper target, at 78° and 90° with respect to the incident proton beam direction. The concrete composition is not given. Data were here scaled to Sv m<sup>2</sup> per proton taking the nominal beam current given in [22], in order to compare them with the attenuation curves provided in the present work. Fig. 32 compares the experimental data at 90° with the present double attenuation function at 80–90° (expression (2), Table 7). The curve is a merge of the first exponential up to a depth of 1 m and the second beyond it. The agreement is good up to 1.5 m, reasonable at 2 m, whilst the calculations underestimate the experimental data by a factor of 3 at 2.5 m and a factor of 4 at 3 m. This may be due to the following reasons: (1) at depths beyond 1.5 m the fast neutron ( $E_n > 20 \text{ MeV}$ ) dose equivalent was not measured directly but only estimated, albeit under reasonable assumptions (as stated in [22]), (2) some additional contribution to the total dose equivalent may come from neutron

Table 10(b)

Comparison of source terms and attenuation lengths in concrete calculated in the present work with literature results (Monte Carlo simulations)

References	$E_p$ (MeV)		Emission angle		Source term (Sv m <sup>2</sup> per proton)		Attenuation length (g cm <sup>-2</sup> )				
	Literature data	Present work	Literature data	Present work	Literature data	Present work	Literature data	Present work			
[23]	150	150	0–15°	0–10°	–	–	91	80.4 ± 0.5			
			15–30°	10–20° <sup>a</sup>	–	–	87	79			
			30–45°	30–40° <sup>a</sup>	–	–	82	76.3			
			45–60°	40–50°	–	–	78	74.3 ± 1.4			
	200	200	0–15°	0–10°	–	–	102	96.6 ± 0.8			
			15–30°	10–20° <sup>a</sup>	–	–	98	93.7			
			30–45°	30–40° <sup>a</sup>	–	–	92	89.1			
			45–60°	40–50°	–	–	87	86.4 ± 0.5			
	250	250	0–15°	0–10°	–	–	109	105.4 ± 1.4			
			15–30°	10–20° <sup>a</sup>	–	–	105	102			
			30–45°	30–40° <sup>a</sup>	–	–	99	96.4			
			45–60°	40–50°	–	–	93	93.5 ± 0.5			
[19]	230	230 <sup>a</sup>	0–10°	0–10°	$(6.6 \pm 0.4) \times 10^{-15}$	$8.40 \times 10^{-15}$	99.1 ± 2.8	100.4			
			40–50°	40–50°	$(2.3 \pm 0.1) \times 10^{-15}$	$9.40 \times 10^{-16}$	89.4 ± 2.1	91			
			85–95°	80–90°	$(1.0 \pm 0.2) \times 10^{-15}$	$6.10 \times 10^{-17}$	53.4 ± 2.6	83.8			
[26]*	100	100	0–5°	0–10°	$9.10 \times 10^{-16}$	$(8.9 \pm 0.4) \times 10^{-16}$	60	59.7 ± 0.2			
	250	250	0–5°	0–10°	$9.60 \times 10^{-15}$	$(9.8 \pm 1.0) \times 10^{-15}$	111	105.4 ± 1.4			
[12]	100	100	20–30°	20–30° <sup>a</sup>	$4.50 \times 10^{-15}$	$3.50 \times 10^{-15}$	114	99.2			
			0–10°	0–10°	$1.10 \times 10^{-15}$	$(8.9 \pm 0.4) \times 10^{-16}$	63.6	59.7 ± 0.2			
			40–50°	40–50°	$4.30 \times 10^{-16}$	$(1.5 \pm 0.1) \times 10^{-16}$	49.1	57.2 ± 0.3			
			80–90°	80–90°	$5.60 \times 10^{-17}$	$(1.1 \pm 0.3) \times 10^{-17}$	38	52.6 ± 0.7			
	150	150	130–140°	130–140°	$3.70 \times 10^{-17}$	$(8.0 \pm 5.1) \times 10^{-18}$	34.6	46.1 ± 2.8			
			0–10°	0–10°	$4.00 \times 10^{-15}$	$(3.0 \pm 0.2) \times 10^{-15}$	89.9	80.4 ± 0.5			
			40–50°	40–50°	$8.80 \times 10^{-16}$	$(3.3 \pm 0.8) \times 10^{-16}$	80.8	74.3 ± 1.4			
			80–90°	80–90°	$1.70 \times 10^{-16}$	$(1.2 \pm 0.3) \times 10^{-17}$	57	70.8 ± 1.3			
	200	200	130–140°	130–140°	$6.10 \times 10^{-17}$	$(2.1 \pm 0.6) \times 10^{-18}$	41.9	61.8 ± 1.1			
			0–10°	0–10°	$5.30 \times 10^{-15}$	$(5.6 \pm 0.4) \times 10^{-15}$	103	96.6 ± 0.8			
			40–50°	40–50°	$1.40 \times 10^{-15}$	$(6.8 \pm 0.5) \times 10^{-16}$	84.5	86.4 ± 0.5			
			80–90°	80–90°	$4.80 \times 10^{-16}$	$(3.7 \pm 0.8) \times 10^{-17}$	61.8	78.3 ± 1.3			
	250	250	130–140°	130–140°	$7.10 \times 10^{-17}$	$(2.8 \pm 2.4) \times 10^{-18}$	42.2	70.0 ± 4.1			
			0–10°	0–10°	$9.00 \times 10^{-15}$	$(9.8 \pm 1.0) \times 10^{-15}$	109	105.4 ± 1.4			
			40–50°	40–50°	$3.30 \times 10^{-15}$	$(1.2 \pm 0.1) \times 10^{-15}$	92.9	93.5 ± 0.5			
			80–90°	80–90°	$6.20 \times 10^{-16}$	$(9.0 \pm 2.5) \times 10^{-17}$	62.8	83.7 ± 2.0			
	400	400 <sup>a</sup>	130–140°	130–140°	$1.50 \times 10^{-16}$	$(6.5 \pm 2.6) \times 10^{-18}$	45.9	79.1 ± 3.4			
			0–10°	0–10°	$1.80 \times 10^{-14}$	$1.50 \times 10^{-13}$	126	112.2			
			40–50°	40–50°	$6.30 \times 10^{-15}$	$9.90 \times 10^{-15}$	99.9	106			
			80–90°	80–90°	$1.70 \times 10^{-15}$	$5.90 \times 10^{-16}$	78.1	100.6			
	[27]	50	50 <sup>a</sup>	130–140°	130–140°	$5.50 \times 10^{-16}$	$3.40 \times 10^{-17}$	60.5	95.9		
				0–5°	0–10°	$6.20 \times 10^{-16}$	$4.10 \times 10^{-16}$	35.1	36.5		
				70	70 <sup>a</sup>	0–5°	0–10°	$1.10 \times 10^{-15}$	$5.80 \times 10^{-16}$	43.2	44.7
				100	100	0–5°	0–10°	$2.30 \times 10^{-15}$	$(8.9 \pm 0.4) \times 10^{-16}$	57	59.7 ± 0.2
[29]	72	72 <sup>a</sup>	0–10°	0–10°	$(3.6 \pm 0.4) \times 10^{-16}$	$6.00 \times 10^{-16}$	49.7 ± 0.5	45.7			
			40–50°	40–50°	$(1.3 \pm 0.1) \times 10^{-16}$	$1.10 \times 10^{-16}$	49.5 ± 0.3	46.6			
			80–90°	80–90°	$(0.4 \pm 0.1) \times 10^{-16}$	$7.30 \times 10^{-18}$	45.7 ± 0.6	44.5			
	250	250	0–10°	0–10°	$(6.4 \pm 0.1) \times 10^{-15}$	$(9.8 \pm 1.0) \times 10^{-15}$	115.4 ± 0.3	105.4 ± 1.4			
			40–50°	40–50°	$(2.1 \pm 0.02) \times 10^{-15}$	$(1.2 \pm 0.1) \times 10^{-15}$	97.4 ± 0.2	93.5 ± 0.5			
			80–90°	80–90°	$(3.8 \pm 0.2) \times 10^{-16}$	$(9.0 \pm 2.5) \times 10^{-17}$	79.1 ± 0.6	83.7 ± 2.0			

All targets are thick iron targets except <sup>a</sup>thick copper.<sup>a</sup> Interpolated/extrapolated data were obtained from Eqs. (3)–(6) (see text, Section 5).

Table 10(c)

Comparison of source terms and attenuation lengths in concrete calculated in the present work with literature results (non-Monte Carlo methods)

References	$E_p$ (MeV)		Emission angle		Source term (Sv m <sup>2</sup> per proton)		Attenuation length (g cm <sup>-2</sup> )	
	Literature data	Present work	Literature data	Present work	Literature data	Present work	Literature data	Present work
[30]	100	100	90°	80–90°	$4.00 \times 10^{-17}$	$(1.1 \pm 0.3) \times 10^{-17}$	50	$52.6 \pm 0.7$
	250	250	90°	80–90°	$6.00 \times 10^{-16}$	$(9.0 \pm 2.5) \times 10^{-17}$	78	$83.7 \pm 2.0$
	400	400 <sup>b</sup>	90°	80–90°	$1.90 \times 10^{-15}$	$5.90 \times 10^{-16}$	89	100.6
[31]	113	113 <sup>b</sup>	7.5°	0–10°	–	–	64.6	66
	113	100	30°	30–40° <sup>b</sup>	–	–	58.3	57.4
			60°	60–70° <sup>b</sup>	–	–	47.3	54.2
	256	250	7.5°	0–10°	–	–	106.9	$105.4 \pm 1.4$
			30°	30–40° <sup>b</sup>	–	–	101	96.4
			60°	60–70° <sup>b</sup>	–	–	79.2	88
[34] <sup>a</sup>			120°	120–130° <sup>b</sup>	–	–	48.2	72.8
	100	100	0°	0–10°	$7.90 \times 10^{-16}$	$(8.9 \pm 0.4) \times 10^{-16}$	60.1	$59.7 \pm 0.2$
			90°	80–90°	$5.20 \times 10^{-16}$	$(1.1 \pm 0.3) \times 10^{-17}$	46.8	$52.6 \pm 0.7$
	150	150	0°	0–10°	$1.40 \times 10^{-15}$	$(3.0 \pm 0.2) \times 10^{-15}$	75.6	$80.4 \pm 0.5$
			90°	80–90°	$8.80 \times 10^{-16}$	$(1.2 \pm 0.3) \times 10^{-17}$	52.2	$70.8 \pm 1.3$
	200	200	0°	0–10°	$2.00 \times 10^{-15}$	$(5.6 \pm 0.4) \times 10^{-15}$	84	$96.6 \pm 0.8$
			90°	80–90°	$1.10 \times 10^{-15}$	$(3.7 \pm 0.8) \times 10^{-17}$	52	$78.3 \pm 1.3$

All targets are thick iron targets.

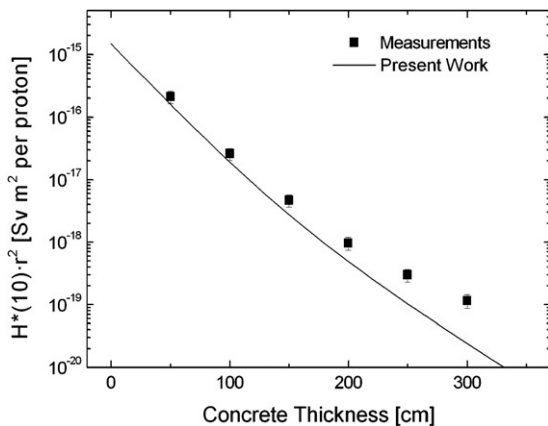
<sup>a</sup> Attenuation lengths are calculated for 4 m thick concrete.<sup>b</sup> Interpolated/extrapolated data were obtained from Eqs. (3)–(6) (see text, Section 5).

Fig. 32. Comparison of experimental data at 90° from [22] with the present double attenuation function at 80–90° (expression (2), Table 7).

scattering in the experimental cave. Measurements performed at 3 m depth could also be affected by uncertainties greater than those stated, because the values were close to detection limits of  $0.1 \mu\text{Sv h}^{-1}$ , as explained in [22]. Nonetheless, the above reasons may still not fully explain the discrepancy at the largest depth.

### 6.2. Comparison with Monte Carlo simulations (Table 10(b))

Data from [23] are Monte Carlo calculations performed with the High Energy Transport Code (HETC-DO) [24], which is based on the Bertini's intranuclear cascade model [25]. The source was placed at the centre of a concrete sphere (whose material composition is different from that used in the present work) and scoring was done inside the material. No results are given for the source term.

The simulations were done with angular bins larger than those used in the present work. Differences are within 15%, and the agreement becomes better with increasing angle and energy: the best agreement is obtained in the 40–50° angular bin for 250 MeV protons, where the attenuation lengths coincide.

Data from [19] are results of Monte Carlo simulations with the LAHET Code System [15]. Differences in the attenuation lengths are within 2% for the forward direction and the 40–50° angular bin, whereas there is 40% discrepancy in the transverse direction. The source terms differ by 20% in the forward direction, by more than a factor of 2 in the 40–50° angular bin and by a factor of 16 in the transverse direction.

Data from [26] are results of Monte Carlo calculations with the FLUKA code, for a slightly different type of concrete. In the forward direction the data are in remarkable agreement with the values of the present work: the source terms agree within 3% and the attenuation lengths within 5%. A comparison with interpolated data at 20–30° shows a discrepancy of 25% on the source term and of 13% on the attenuation length.

Data from [12] deserve a specific comment, as they are results of FLUKA simulations in exactly the same geometry of the present work, but scoring particles at different depths inside the shield in all angular bins. Except for the forward angles, the attenuation lengths are systematically lower than those from the present calculations (partly compensated by higher values in the source terms). This is explained by the fact that, due to the much lower computing power available in the mid-nineties with respect to present, the simulations were at that time performed in two steps. First the neutron energy distributions were generated from the target, followed by a second step in which neutrons were transported through the shield. Most likely

the high-energy component in the neutron energy distributions was undersampled in the first step, which in turn means a faster attenuation in the shield.

Data from ref [27] are FLUKA simulations with protons in the energy range 10–100 MeV and a geometry set up very similar to that of the present (and earlier [12]) work. The source neutrons produced in the iron target were replaced by tabulated neutron yield data from ICRU Report 63 [28], and the complete concrete spherical shell was simulated for the neutron transport. The only direct comparison can be made at 100 MeV in the forward direction, for which attenuation lengths agree within 5% while source terms differ by a factor of 2.6. This is probably due to the fact that the present simulations reach a depth of 6 m in concrete: as a consequence the neutron spectrum can harden a little more, with the consequence of rising the attenuation length and reducing the source term.

Data from [29] are MCNPX simulations in a geometry set-up very close to the one implemented in the present work and in ref [12]. Attenuation lengths agree within 10%, whereas as usual the source terms differ more. The discrepancies may be due to the different cross section libraries implemented in MCNPX for protons interaction with iron.

### 6.3. Comparison with other (non Monte Carlo) methods (Table 10(c))

Tesch [30] reports parameters for lateral shielding obtained by fitting data from the literature. According to the energy, the agreement with the present results is within 12% for the attenuation length. For the source term there is a discrepancy of a factor of 3.6 at 100 MeV and at 400 MeV, and of a factor of 6.6 at 250 MeV.

Kato and Nakamura [31] provides only values of the attenuation length obtained transporting measured neutron spectra from [14,32,33] with the ANISN one-dimensional discrete ordinate code. There is a good agreement with the present results in the forward direction and for 30° (within 5%), whereas the discrepancy increases with increasing emission angle, but it is particularly large only at 120°.

Maiti et al. [34] proposes a mathematical tool for predicting attenuation lengths and source terms for concrete in the proton energy range 25–200 MeV, both in the forward and lateral directions. The attenuation length is calculated as a function of incident proton energy and concrete thickness, the source term as a function of target material and proton energy. Differences with the present results in the attenuation length are within 15% in the forward direction but are as large as 35% in the transverse direction: the comparison has been made taking the values proposed in [34] after 4 meters of concrete, in order to make a comparison for deep penetration in the shield. Values in the source term show larger discrepancies: less than a factor of 3 in the forward direction, more than an order of magnitude in the lateral direction. Figs. 33 and 34 compare

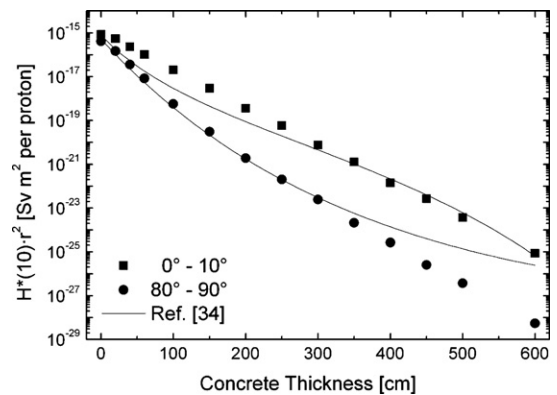


Fig. 33. Attenuation of total dose equivalent in ordinary concrete for 100 MeV protons on a thick iron target: comparison between results from the present work and the analytical method of [34]. The statistical uncertainties of each data point are smaller than the size of the symbols.

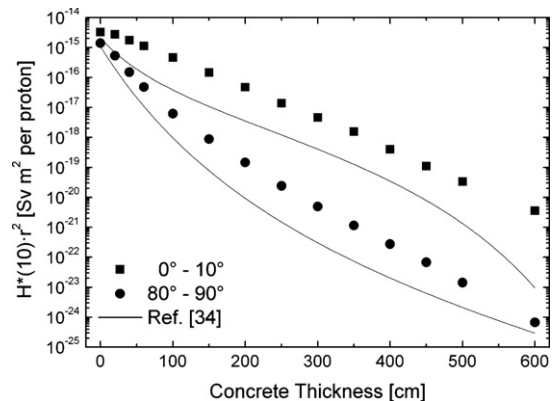


Fig. 34. Attenuation of total dose equivalent in ordinary concrete for 200 MeV protons on a thick iron target: comparison between results from the present work and the analytical method of [34]. The statistical uncertainties of each data point are smaller than the size of the symbols.

the results of the present work with the predictions of the model of [34].

## 7. Conclusions

This paper has revised and improved previous shielding calculations for concrete. These data will be complemented by shielding parameters for iron in a forthcoming paper [7]. Concrete is the most common material used in accelerator shielding, but iron is also used, normally in combination with concrete, for which very few data – both experimental and computational – are available in the literature. In the present paper an effort has been made to obtain a consistent set of source terms and attenuation lengths to be used in the shielding design of intermediate energy proton accelerators. A detailed analysis of the assumptions made has shown that the approximation employed in the simulations should only introduce marginal variations with respect to a real, slab geometry. The present data should be of help for shielding studies and reduce to a minimum the need for long and complex Monte Carlo calculations. The smooth behaviour of  $\lambda$  and  $H_0$  versus proton energy and polar

angle allows to interpolate the data for application at any energy in the 100–250 MeV range, and to a certain extent extrapolate outside this energy range. Data for thin shields (that is, the attenuation length determined by the first exponential in expression (2)) can be of interest under specific circumstances, for example a barrier designed to shield an area with a very low occupancy factor – or no occupancy at all – or conceived to shield an accelerator running at very low beam current.

Literature data are sparse and specific to given beam conditions and geometries. An extensive comparison of source terms and attenuation lengths obtained in the present work with published data shows the comparatively wide range of variability in the results, which reflects the large differences in the geometrical configurations (experimental or computational), material composition and techniques used. The concrete composition may in particular have a substantial impact on the attenuation properties of a barrier. Concrete compositions may vary significantly, particularly in the content of hydrogen (from 0.39 to  $1.9 \times 10^{21}$  atoms  $\text{cm}^{-3}$ ), carbon (from 0.05 to 2.02) and silicon (from 0.17 to 2.08) when comparing the composition used in the present work and those found in the literature [18,19,23,26,31]. To disentangle the influence of the concrete composition from all other effects one would need to perform a dedicated set of simulations or experimental measurements by only varying the concrete type while keeping all other parameters fixed (for example, [35]). Nonetheless, apart from some exceptions, the overall agreement amongst the various sets of data can be regarded as acceptable.

## Acknowledgement

The authors wish to thank Alfredo Ferrari (CERN) for useful discussions.

## References

- [1] <http://ptcog.web.psi.ch/>.
- [2] L. Arnaudon et al., Linac4 Technical Design Report, Report CERN-AB-2006-084-ABP/RF, 2006.
- [3] F. Gerigk et al., Conceptual Design of the SPL II, CERN-2006-006, 2006.
- [4] A.H. Sullivan, A Guide to Radiation and Radioactivity Levels Near High Energy Particle Accelerators, Nuclear Technology Publishing, Ashford, Kent, TN23 1JW, England, 1992.
- [5] M. Magistris, M. Silari, H. Vincke, Radiat. Protect. Dosim. 115 (2005) 553.
- [6] R.H. Thomas, G.R. Stevenson, Radiological Safety Aspects of the Operation of Proton Accelerators, Technical Report Series No. 283, IAEA, Vienna, 1988.
- [7] S. Agosteo, M. Magistris, A. Mereghetti, M. Silari, Z. Zajacova, Shielding data for 100–250 MeV proton accelerators: attenuation of secondary radiation in thick iron and concrete/iron shields, Nucl. Instr. and Meth. B, submitted for publication.
- [8] A. Fassò, A. Ferrari, J. Ranft, P.R. Sala, FLUKA: a Multi-Particle Transport Code, CERN-2005-10 (2005), INFN/TC\_05/11, SLAC-R-773.
- [9] A. Fassò et al., The Physics Models of FLUKA: Status and Recent Developments, Computing in High Energy and Nuclear Physics 2003 Conference (CHEP2003), La Jolla, CA, USA, March 24–28, 2003, (paper MOMT005), eConf C0303241 (2003). arXiv:hep-ph/0306267.
- [10] International Commission on Radiological Protection, ICRP Publication 74, Conversion Coefficients for Use in Radiological Protection Against External Radiation, Pergamon Press, 1997.
- [11] M. Pelliccioni, Radiat. Protect. Dosim. 88 (2000) 279.
- [12] S. Agosteo, A. Fassò, A. Ferrari, P.R. Sala, M. Silari, P. Tabarelli de Fatis, Nucl. Instr. and Meth. B 114 (1996) 70.
- [13] International Commission on Radiation Units and Measurements, Report No. 49, Bethesda, Maryland, USA, 1993.
- [14] M.M. Meier, C.A. Goulding, G.L. Morgan, J.L. Ullmann, Nucl. Sci. Eng. 104 (1990) 339.
- [15] R.E. Prael, H. Lichtenstein, User Guide to LCS: the LAHET Code System, Los Alamos Report LA-UR-89-3014, 1989.
- [16] S. Agosteo, T. Nakamura, M. Silari, Z. Zajacova, Nucl. Instr. and Meth. B 217 (2004) 221.
- [17] S. Agosteo, G. Fehrenbacher, M. Silari, Nucl. Instr. and Meth. B 226 (2004) 231.
- [18] J.V. Siebers, P.M. DeLuca Jr., D.W. Pearson, Nucl. Sci. Eng. 122 (1996) 258.
- [19] H.B. Knowles, J.L. Orthel, B.W. Hill, in: Proc. of the 1993 Particle Accelerator Conference, Washington DC, May 17–20, 1993, IEEE (1993), p. 1762.
- [20] International Commission on Radiation Units and Measurements, Report No. 36, Bethesda, Maryland, USA, 1983.
- [21] A. Mazal et al., Radiat. Protect. Dosim. 70 (1997) 429.
- [22] S. Teichmann, B. Amrein, J. Gerig, W. Hajdas, H. Temnitzer, in: Proc. of the AEN/NEA Specialists' Meeting on Shielding Aspects of Accelerators, Targets and Irradiation Facilities, Stanford Linear Accelerator Center (USA), 10–12 April 2002, NEA/OECD (2002).
- [23] W.K. Hagan, B.L. Colborn, T.W. Armstrong, Nucl. Sci. Eng. 98 (1988) 272.
- [24] T.W. Armstrong, C. Chandler, Nucl. Sci. Eng. 49 (1972) 110.
- [25] H.W. Bertini, Phys. Rev. 6 (1972) 631.
- [26] A. Fassò, A. Ferrari, G.R. Stevenson, in: Proc. of the AEN/NEA Specialists' Meeting on Shielding Aspects of Accelerators, Targets and Irradiation Facilities, Arlington (Texas), 28–29 April 1994, NEA/OECD (1995), p. 155.
- [27] C.C. Chen, R.J. Sheu, S.H. Jiang, Radiat. Protect. Dosim. 116 (2005) 245.
- [28] International Commission on Radiation Units and Measurements, Report No. 63 Bethesda, Maryland, USA., 2000.
- [29] S. Teichmann, in: Proc. of the AEN/NEA Specialists' Meeting on Shielding Aspects of Accelerators, Targets and Irradiation Facilities, Pohang Accelerator Laboratory, 22–24 May 2006, NEA/OECD (2006) (in press).
- [30] K. Tesch, Radiat. Protect. Dosim. 11 (1985) 165.
- [31] T. Kato, T. Nakamura, Nucl. Instr. and Meth. B 174 (2001) 482.
- [32] T. Kurosawa, T. Nakao, T. Nakamura, Y. Uwamino, T. Shibata, N. Nakanishi, A. Fukumura, K. Murakami, Nucl. Sci. Eng. 132 (1999) 30.
- [33] M.M. Meier, W.B. Amian, C.A. Goulding, G.L. Morgan, C.E. Moss, Nucl. Sci. Eng. 102 (1989) 310.
- [34] M. Maiti, M. Nandy, S.N. Roy, P.K. Sarkar, Nucl. Instr. and Meth. B 226 (2004) 585.
- [35] K.R. Kase, W.R. Nelson, A. Fassò, J.C. Liu, X. Mao, T.M. Jenkins, J.H. Kleck, Health Phys. 84 (2003) 180.